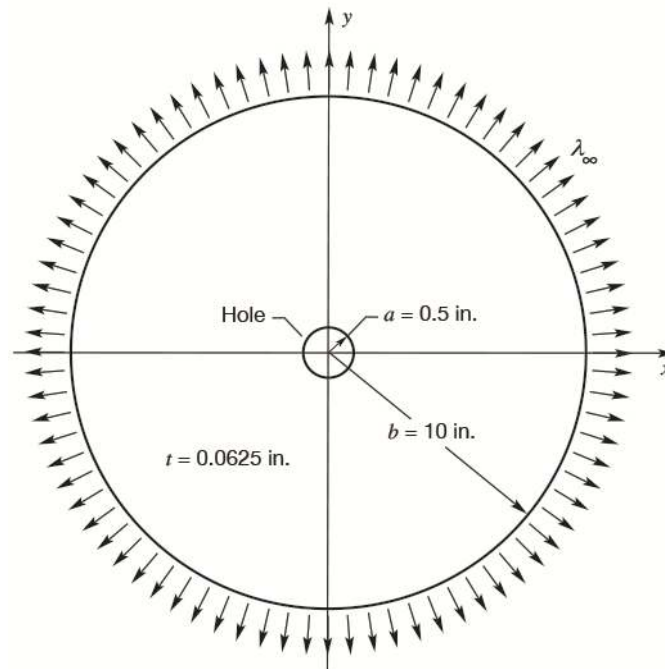# Non-Classical Stress Concentration Behavior in a Radially Stretched Hyperelastic Sheet Containing a Circular Hole

William L. Ko
NASA Armstrong Flight Research Center, Edwards, California

Shun-Fat Lung
Jacobs Technology, Edwards. California

August 2017

NASA STI Program ... in Profile

Since its founding, NASA has been dedicated to the advancement of aeronautics and space science. The NASA scientific and technical information (STI) program plays a key part in helping NASA maintain this important role.

The NASA STI program operates under the auspices of the Agency Chief Information Officer. It collects, organizes, provides for archiving, and disseminates NASA's STI. The NASA STI program provides access to the NTRS Registered and its public interface, the NASA Technical Reports Server, thus providing one of the largest collections of aeronautical and space science STI in the world. Results are published in both non-NASA channels and by NASA in the NASA STI Report Series, which includes the following report types:

- TECHNICAL PUBLICATION. Reports of completed research or a major significant phase of research that present the results of NASA Programs and include extensive data or theoretical analysis. Includes compilations of significant scientific and technical data and information deemed to be of continuing reference value. NASA counter-part of peer-reviewed formal professional papers but has less stringent limitations on manuscript length and extent of graphic presentations.

- TECHNICAL MEMORANDUM. Scientific and technical findings that are preliminary or of specialized interest, e.g., quick release reports, working papers, and bibliographies that contain minimal annotation. Does not contain extensive analysis.

- CONTRACTOR REPORT. Scientific and technical findings by NASA-sponsored contractors and grantees.

- CONFERENCE PUBLICATION. Collected papers from scientific and technical conferences, symposia, seminars, or other meetings sponsored or co-sponsored by NASA.

- SPECIAL PUBLICATION. Scientific, technical, or historical information from NASA programs, projects, and missions, often concerned with subjects having substantial public interest.

- TECHNICAL TRANSLATION. English-language translations of foreign scientific and technical material pertinent to NASA's mission.

Specialized services also include organizing and publishing research results, distributing specialized research announcements and feeds, providing information desk and personal search support, and enabling data exchange services.

For more information about the NASA STI program, see the following:

- Access the NASA STI program home page at http://www.sti.nasa.gov

- E-mail your question to help@sti.nasa.gov

- Phone the NASA STI Information Desk at 757-864-9658

- Write to:
  NASA STI Information Desk
  Mail Stop 148
  NASA Langley Research Center
  Hampton, VA 23681-2199

NASA/TM—2017–219527
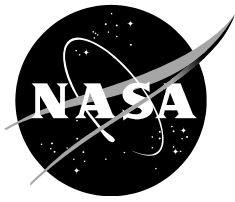
Non-Classical Stress Concentration Behavior in a Radially Stretched Hyperelastic Sheet Containing a Circular Hole

William L. Ko
NASA Armstrong Flight Research Center, Edwards, California

Shun-Fat Lung
Jacobs Technology, Edwards, California

August 2017

Acknowledgments

Table of Contents

Abstract

Non-classical stress concentration behavior in a stretched circular hyperelastic sheet (outer radius $b = 10$ in., thickness $t = 0.0625$ in.) containing a central hole (radius $a = 0.5$ in.) was analyzed. The hyperelastic sheet was subjected to different levels of remote radial stretchings. Nastran large-strain large-deformation analysis and the Blatz-Ko large deformation theory were used to calculate the equal-biaxial stress concentration factors K. The results show that the values of K calculated from the Blatz-Ko theory and Nastran are extremely close. Unlike the classical linear elasticity theory, which gives the constant $K = 2$ for the equal-biaxial stress field, the hyperelastic K values were found to increase with increased stretching and can exceed the value $K = 6$ at a remote radial extension ratio of 2.35. The present K-values compare fairly well with the K-values obtained by previous works. The effect of the hole-size on K-values was investigated. The values of K start to decrease from a hole radius $a = 0.125$ in. down to $K = 1$ (no stress concentration) as a shrinks to $a = 0$ in. (no hole). Also, the newly introduced stretch and strain magnification factors $\{K_\lambda, K_\varepsilon\}$ are also material- and deformation-dependent, and can increase from linear levels of $\{1.0, 4.0\}$ and reaching $\{3.07, 4.61\}$, respectively at a remote radial extension ratio of 2.35.

Nomenclature

a	hole radius, in.
b	remote radius, in.
C_{ik}	$\equiv \begin{pmatrix} \lambda_1^2 & 0 & 0 \\ 0 & \lambda_2^2 & 0 \\ 0 & 0 & \lambda_3^2 \end{pmatrix}$, Cauchy-Green deformation tensor in principal axes
C_1	$\equiv \dfrac{\partial W}{\partial I_1}$, Mooney-Rivlin constant
C_2	$\equiv \dfrac{\partial W}{\partial I_2}$, Mooney-Rivlin constant (J_3-dependent)
d	mathematical symbol for differentiation
E	Young's modulus, lb/in^2
I_1	$\equiv Tr C_{ik} = C_{ii} = \lambda_1^2 + \lambda_2^2 + \lambda_3^2$, first invariant of C_{ik}
I_2	$\equiv \sum\limits_{i \neq k} C_{ii} C_{kk} = \dfrac{1}{2}\left(I_1^2 - C_{ik} C_{ki} \right) = \lambda_1^2 \lambda_2^2 + \lambda_2^2 \lambda_3^2 + \lambda_3^2 \lambda_1^2$, second invariant of C_{ik}
I_3	$\equiv Det C_{ik} = \lambda_1^2 \lambda_2^2 \lambda_3^2$, third invariant of C_{ik}
J_1	$\equiv I_1 = C_{ii} = \lambda_1^2 + \lambda_2^2 + \lambda_3^2$, first invariant
J_2	$\equiv \dfrac{I_2}{I_3} = (C^{-1})_{ii} = \dfrac{1}{\lambda_1^2} + \dfrac{1}{\lambda_2^2} + \dfrac{1}{\lambda_3^2}$, modified second invariant
J_3	$\equiv \sqrt{I_3} = \sqrt{Det C_{ik}} = \lambda_1 \lambda_2 \lambda_3 = \dfrac{\text{Deformed volume}}{\text{Undeformed volume}}$, modified third invariant
i, j	$= 1,2,3$, indices

K $\qquad \equiv \dfrac{\sigma_{\max}\lambda_{\max}}{\sigma_{\infty}\lambda_{\infty}}$, stress concentration factor

K_{λ} $\qquad \equiv \dfrac{\lambda_{\max}}{\lambda_{\infty}}$, stretch magnification factor

K_{ε} $\qquad \equiv \dfrac{\varepsilon_{\max}}{\varepsilon_{\infty}}$, strain magnification factor

r $\qquad$ radial coordinate, in.

t $\qquad$ thickness, in.

UAV $\qquad$ unmanned aerial vehicle

W $\qquad$ strain energy density function, in-lb/in^3

W_1 $\qquad \equiv \dfrac{\partial W}{\partial J_1} = C_1$, first strain energy gradients (material constant), lb/in^2

W_2 $\qquad \equiv \dfrac{\partial W}{\partial J_2} = C_2 J_3$, second strain energy gradient (material constant), lb/in^2

W_3 $\qquad \equiv \dfrac{\partial W}{\partial J_3}$, third strain energy gradient, lb/in^2

ε $\qquad = \lambda - 1$, strain, in/in

ε_{e-bi} $\qquad$ equal-biaxial strain, in/in

$\varepsilon_{\max}$ $\qquad$ maximum tangential strain at hole boundary, in/in

ε_{uni} $\qquad$ uniaxial strain, in/in

ε_{θ} $\qquad$ tangential strain, in/in

ε_{∞} $\qquad$ biaxial strain at remote boundary, in/in

$\lambda_1, \lambda_2, \lambda_3$ $\qquad$ extension ratios in 1, 2, 3-directions

λ $\qquad = 1 + \varepsilon$, extension ratio in loading direction

λ_{lat} $\qquad$ extension ratio in lateral directions for uniaxial tension

λ_{th} $\qquad$ extension ratio in thickness direction for biaxial tension

λ_r $\qquad = d\rho(r)/dr$, radial extension ratio

λ_{θ} $\qquad = \rho(r)/r$ tangential extension ratio

λ_{∞} $\qquad \equiv \lambda_r(b) = (d\rho/dr)_{r=b}$, remote ($r = b$) radial extension ratio

$\lambda_{\max}$ $\qquad \equiv \lambda_{\theta}(a) = (\rho/r)_{r=a}$, hole-boundary ($r = a$) tangential extension ratio

μ $\qquad$ shear modulus at small strain ($\lambda_i \to 1$), lb/in^2

v $\qquad \equiv -\dfrac{\ln\lambda_{lat}}{\ln\lambda}$, modified Poisson's ratio for large deformations

ρ $\qquad$ deformed length of r, in.

σ_{uni} $\qquad$ uniaxial engineering stress (Biot stress) in reference to an undeformed cross section, lb/in^2

σ_{s-bi} $\qquad$ strip-biaxial engineering stress in reference to an undeformed cross section, lb/in^2

σ_{e-bi} $\qquad$ equal-biaxial engineering stress in reference to an undeformed cross section, lb/in^2

σ_r $\qquad$ engineering stress in a radial direction, lb/in^2

σ_{θ} $\qquad$ engineering stress in a tangential direction, lb/in^2

2

σ_{∞} $\equiv \sigma_r(b)$, remote ($r = b$) radial engineering stress, lb/in^2

σ_{max} $\equiv \sigma_{\theta}(a)$, hole boundary ($r = a$) tangential engineering stress, lb/in^2

$\bar{\sigma}_r$ radial true stress (Cauchy stress) in reference to deformed cross section, lb/in^2

$\bar{\sigma}_{uni}$ $= (\sigma_{uni}\lambda)/J_3$, uniaxial true stress (Cauchy stress) in reference to deformed cross section, lb/in^2

$\bar{\sigma}_{\theta}$ tangential true stress (Cauchy stress) in reference to deformed cross section, lb/in^2

Introduction

Hyperelastic (rubber-like) materials have wide applications (for example, automobile tires, rubber hoses, shock absorbers, inflatable unmanned aircraft, hovercraft skirts, et cetera). In the major aerospace applications, rubber materials are traditionally used as fuels in solid rocket motors (for example, Space Shuttle solid rocket boosters, surface-to-air, and air-to-air missiles). Rubber burns very slowly, however, when mixed with oxidizer particles (for example, ammonium perchlorate oxidizer particles) to form composite solid propellants, the solid rocket propellants can burn very rapidly to generate tremendous thrust. For example, each Space Shuttle solid rocket booster could generate approximately 3,300,000 lb thrust at lift-off. Because of particle inclusions, the composite solid propellant has stress concentration problems. For example, the star tips of the star-grain (fig. 1), when ignited, could be the potential crack initiation sites because of tensile stress concentration induced by the chamber pressure.

Because of increasing aerospace applications of hyperelastic materials [For example, transition flaps, launch vehicle engine vibration damping, structural flutter suppressions, inflatable wing skins of an unmanned aerial vehicle (UAV), et cetera.], there is a need to fully understand fundamental mechanical behavior of such materials. The hyperelastic membrane has no compressive strength. When applied to inflatable aircraft skins, or transition flaps for noise reduction (ref. 1), the hyperelastic skins must be pre-stretched to maintain shapes. When a sharp particle strikes and penetrates a stretched hyperelastic sheet, a small hole generated could cause a very high stress concentration around the hole boundary. An excessive high stress concentration can cause instant tearing failure. A pressurized balloon is a good example of a highly stretched hyperelastic skin. With a simple contact with a sharp object, the balloon can burst instantly because the pinhole created induces a high stress concentration at the pinhole boundary causing the hole boundary material to reach failure stress.

In general, uniaxial stress-strain data are used as a basis to describe the mechanical behavior of hyperelastic materials. However, in aerospace applications, hyperelastic skins are usually under biaxial stress fields. Therefore, there is a need to fully understand the biaxial stress-strain behavior and non-classical stress concentration behavior of the stretched hyperelastic materials.

In the classical linear elasticity theory, the stress concentration factor K around a hole is $K = 3$ under the uniaxial stress field, and $K = 2$ under the equal-biaxial stress field. Those K values are independent of material properties and independent of stretching (ref. 2). However, for large deformations of a hyperelastic sheet with a hole, the value of K can be dependent of material properties and hole-size, and can increase with increased stretching.

This technical report will analyze the non-classical stress concentration problem in a radially stretched circular hyperelastic sheet containing a central circular hole made of widely-used Mooney material (refs. 3, 4), and will theoretically confirm that the equal-biaxial stress concentration factor K is material, hole-size, and stretch dependent.

Nastran (ref. 5) large-strain large deformation analysis (using fine mesh) and the Blatz-Ko large deformation theory (refs. 6, 7) were used to calculate the hyperelastic equal-biaxial stress concentration factors K. The results show that the values of K calculated from Nastran and from the Blatz-Ko large deformation theory (refs. 6, 7) are extremely close, and compare fairly well with the K-values obtained in other analyses (refs. 8–11).

Unlike linear elasticity theory, which gives the constant $K = 2$ for the equal-biaxial stress field, the equal-biaxial stress concentration factor K for hyperelastic materials was found to be material-dependent, hole-size-dependent, and deformation-dependent, and can increase with increased stretching, reaching the values several times that of $K = 2$ (linear case).

Also, in the report, the stretch- and strain-magnification factors for hyperelastic materials are introduced, and the material- and deformation-dependent behaviors are discussed.

Material Considered

This section describes the historical Mooney material, which was used in the current biaxial stress concentration analysis, and presents some comments about using the reduced plot to obtain hyperelastic material constants.

Mooney Material

For the current rudimentary stress-concentration analysis, the historical Mooney material (W_1 = 18.35 lb/in^2, W_2 = 1.835lb/in^2) (refs. 3, 4) was chosen. The two material constants $\{W_1, W_2\}$ are the two types of strain energy gradients defined as $W_1 \equiv \partial W/\partial J_1 = \partial W/\partial I_1 = C_1$; $J_1 = I_1 = \lambda_1^2 + \lambda_2^2 + \lambda_3^2$ and $W_2 \equiv \partial W/\partial J_2 = (\partial W/\partial I_2)J_3 = C_2 J_3$; $J_2 \equiv 1/\lambda_1^2 + 1/\lambda_2^2 + 1/\lambda_3^2$; $I_2 = \lambda_1^2\lambda_2^2 + \lambda_2^2\lambda_3^2 + \lambda_3^2\lambda_1^2$; $J_3 \equiv \sqrt{I_3} = \sqrt{\mathrm{Det}C_{ik}} = \lambda_1\lambda_2\lambda_3$.

Figure 2 shows the uniaxial stress-strain curve of the Mooney material, and figure 3 shows the reduced plot, $\dfrac{\sigma_{uni}\lambda}{\lambda^2 - 1/\lambda}$ against $1/\lambda$, using the data of figure 2 for obtaining the material constants (W_1 = 18.35 lb/in^2, W_2 = 1.835lb/in^2) lb/in^2 through linear curve fitting. Because the Mooney material was widely used by earlier researchers (refs. 8–11) in the similar biaxial stress concentration studies, by using the same Mooney material in the current biaxial stress concentration analysis, the results can be easily compared with the earlier results (refs. 8–11). Therefore, one can examine the consistency of the biaxial stress concentration behavior of the same hyperelastic material.

Comments on the Reduced Plot

It is important to mention that in the reduced data plotting, $\dfrac{\sigma_{uni}\lambda}{\lambda^2 - 1/\lambda}$ against $1/\lambda$ shown in figure 3, the value of $\dfrac{\sigma_{uni}\lambda}{\lambda^2 - 1/\lambda}$ at the limit $\lambda = 1$ ($\sigma_{uni} = 0$) is not zero nor indeterminate $(0/0)$, but has a finite value equal to shear modulus $\mu\, [= (2W_1 + 2W_2)]$ of incompressible materials (v = 0.5). Namely, by expanding $\dfrac{\sigma_{uni}\lambda}{\lambda^2 - 1/\lambda}$ in the neighborhood of $\lambda \to 1$ (that is , $\varepsilon \to 0$), the limit value $\left(\dfrac{\sigma_{uni}\lambda}{\lambda^2 - 1/\lambda}\right)_{\lambda=1}$ will become shear modulus μ of incompressible materials (v = 0.5) according to the following expanded equation (1):

$$\frac{\sigma_{uni}\lambda}{\lambda^2 - 1/\lambda} \xrightarrow[\substack{\varepsilon \to 0}]{\lambda \to 1} \frac{\overbrace{E\varepsilon}^{\sigma_{uni}}(1+\varepsilon)}{(1+\varepsilon)^2 - (1+\varepsilon)^{-1}} = \frac{\overbrace{2\mu(1+v)}^{E}\varepsilon(1+\varepsilon)}{(1+2\varepsilon+...)-(1-\varepsilon+...)} \xrightarrow{v=0.5} \frac{3\mu\varepsilon}{3\varepsilon} = \mu \qquad (1)$$

4

In general, the reduced plot (similar to figure 3) for any hyperelastic material is nonlinear, but contains a large linear region. For the linear curve fitting to determine the material constants $\{2W_1, 2W_2\}$, one can use the value of μ calculated from equation (1) to estimate the location of the vertical intercept $(2W_1 + 2W_2)$ at $1/\lambda = 1$ of the curve-fitting straight line (similar to figure 3).

As an example, using the value of elastic modulus $E = 117.92$ lb/in^2, determined from the initial slope of the uniaxial stress-strain curve of figure 1, the limit value $\left(\dfrac{\sigma_{uni} \lambda}{\lambda^2 - 1/\lambda} \right)_{\lambda=1} (= \mu)$ for the incompressible Mooney material can be calculated as: $\mu = \left[\dfrac{E}{2(1+v)} \right]_{v=0.5} = \dfrac{117.92}{3} = 39.31 \text{lb/in}^2$, which is extremely close to the value of $(2W_1 + 2W_2) = 40.37$ lb/in^2 (vertical intercept at $1/\lambda = 1$) determined from linear curve fitting shown in figure 2.

Descriptions of the Problem

For the stress concentration analysis, the problem considered is a circular hyperelastic sheet containing a central circular hole subjected to remote radial stretching (fig. 4). Figure 4 shows the geometry of the hyperelastic sheet with a boundary radius of $b = 10$ in., thickness $t = 0.0625$ in., and hole radius $a = 0.5$ in., and is made of Mooney material ($W_1 = 18.35$, $W_2 = 1.835$) lb/in^2. Figure 5 shows the Nastran (ref. 5) finite-element quarter model for the case $b = 10$ in. The case of $b = 5$ in. was first considered, however, an accurate remote equal-biaxial stress field could not be obtained because $b = 5$ in. was too small. Therefore, b had to be increased to $b = 10$ in. in the current analysis. At $b = 10$ in. the remote boundary will be practically under an equal-biaxial stress field. The hyperelastic sheet was subjected to different levels of remote radial stretching ($\lambda_\infty = 1.25$, 1.50, 1.70, 1.98, 2.10, 2.35) (used by earlier authors, refs. 7–10). Nastran large-strain large-deformation analysis was then used to study the effect of stretching on the stress concentration factor K. Also, the Blatz-Ko large deformation theory (ref. 6, 7) was used to calculate the stress concentration factors K and compared with the corresponding Nastran-calculated K values.

Deformation Equations

If radial length r of the hyperelastic circular sheet with a hole is radially deformed to $\rho(r)$, the radial and tangential extension ratios $\{\lambda_r, \lambda_\theta\}$ can be expressed respectively with equation (2) (refs. 2, 3):

$$\lambda_r(r) = \frac{d\rho(r)}{dr} \qquad ; \qquad \lambda_\theta(r) = \frac{\rho(r)}{r} \tag{2}$$

At the deformed hole boundary, the tangential extension ratio $\lambda_\theta(a)$ can be written as equation (3):

$$\lambda_{max} \equiv \lambda_\theta(a) = \frac{\rho(a)}{a} \tag{3}$$

At the deformed remote boundary, the radial and tangential extension ratios $\{\lambda_r(b), \lambda_\theta(b)\}$ become identical if b is sufficiently large ($b \geq 10$ in.). Namely, one can establish equation (4):

$$\lambda_\infty \equiv \lambda_r(b) = \left(\frac{d\rho}{dr}\right)_{r=b} \xrightarrow{\ b \to \infty\ } \frac{\rho(b)}{b} = \lambda_\theta(b) \tag{4}$$

The remote radial extension ratio λ_∞ is to be specified, but the tangential extension ratio λ_{max} at deformed hole-boundary must be calculated from equation (3) by inputting the experimentally measured deformed hole radius $\rho(a)$.

For a special case when the hole shrinks to zero, and the specimen degenerates into a continuous sheet, the radial and tangential extension ratios become identical as shown in equation (5):

$$\lambda_r(r) = \frac{d\rho(r)}{dr} = \frac{\rho(r)}{r} = \lambda_\theta(r) \tag{5}$$

Thus, the strain field becomes the equal-biaxial strain field everywhere in the continuous specimen.

Large Deformation Theory

This section presents the general form of the Blatz-Ko stress-difference equation (refs. 6, 7), and its special forms written respectively for the uniaxial, strip-biaxial, and equal-biaxial stress fields for applications to the calculations of the biaxial stress concentration factor.

Stress-Difference Equations

By taking the difference between stresses in i and j directions, one can eliminate the terms containing $W_3(\equiv \partial W/\partial J_3)$ in which $J_3 = \sqrt{I_3} = \sqrt{\mathrm{Det}C_{ik}} = \lambda_1\lambda_2\lambda_3$. The resulting Blatz-Ko stress difference equation has the following form shown in equation (6) (refs. 6, 7):

$$\frac{\sigma_i\lambda_i - \sigma_j\lambda_j}{\lambda_i^2 - \lambda_j^2} = 2W_1 + \frac{2W_2}{\lambda_i^2\lambda_j^2} \quad ; \quad (i,j = 1,2,3)\ (i,j \text{ not summed}) \tag{6}$$

In equation (6), $\{\sigma_i, \sigma_j\}$ and $\{\lambda_i, \lambda_j\}$ are respectively the engineering stresses (Biot stresses) and extension ratios in $(i,j)(=1,2,3)$ directions, and $\{W_1(=\partial W/\partial J_1); W_2(=\partial W/\partial J_2)\}$ are the material constants. For incompressible materials $(J_3 = \sqrt{I_3} = \lambda_1\lambda_2\lambda_3 = 1)$, the quantities $\{(\sigma_i\lambda_i), (\sigma_j\lambda_j)\}$ in equation (6) will become the true stresses (Cauchy stresses) respectively in $(i,j)(=1,2,3)$ directions. Equation (6) is applicable to both compressible (for example, foamed rubbers) and incompressible hyperelastic materials. The stress-difference equations (6) can now be written for three major stress fields (uniaxial tension, strip-biaxial tension, and equal-biaxial tension) for incompressible materials $(J_3 = 1)$ as presented below.

1. Uniaxial Tension

For uniaxial tension ($\sigma_1 = \sigma_{uni}, \sigma_2 = \sigma_3 = 0$; $\lambda_1 = \lambda$, $\lambda_2 = \lambda_3 = \lambda_{lat}$), the stress difference equation (6) for incompressible materials ($J_3 = \lambda_1 \lambda_2 \lambda_3 = \lambda \lambda_{lat}^2 = 1$) takes on the form of equation (7) (refs. 6, 7):

$$\frac{\sigma_{uni} \lambda}{\lambda^2 - 1/\lambda} = 2W_1 + \frac{2W_2}{\lambda} \tag{7}$$

By plotting $\dfrac{\sigma_{uni} \lambda}{\lambda^2 - 1/\lambda}$ against $1/\lambda$ for the uniaxial case, one can curve-fit the data points with a linear trend line, and determine $2W_1$ from the vertical intercept at $1/\lambda = 0$ and $(2W_1 + 2W_2)$ from the vertical intercept at $1/\lambda = 1$ (fig. 3).

2. Strip-Biaxial Tension

For strip-biaxial tension ($\sigma_1 = \sigma_{s-bi}$, $\sigma_2 \neq 0$, $\sigma_3 = 0$; $\lambda_1 = \lambda$, $\lambda_2 = 1$, $\lambda_3 = \lambda_{th}$), the stress difference equation (6) for incompressible materials ($J_3 = \lambda_1 \lambda_2 \lambda_3 = \lambda \lambda_{th} = 1$) takes on the form of equation (8) (refs. 6, 7):

$$\frac{\sigma_{s-bi} \lambda}{\lambda^2 - 1/\lambda^2} = 2W_1 + 2W_2 \tag{8}$$

By plotting $\sigma_{s-bi} \lambda$ against $(\lambda^2 - 1/\lambda^2)$, one can curve-fit the data points with a linear trend line and determine the summation of $(2W_1 + 2W_2)$ from the slope of the plot, but $2W_1$ and $2W_2$ cannot be determined separately from the plot. Keep in mind that in the biaxial balloon test, the stress field near the ballooned specimen boundary will be under the strip-biaxial stress field, and can be described by equation (8).

3. Equal-Biaxial Tension

For the equal-biaxial tension ($\sigma_1 = \sigma_2 = \sigma_{e-bi}$, $\sigma_3 = 0$; $\lambda_1 = \lambda_2 = \lambda$, $\lambda_3 = \lambda_{th}$), the stress difference equation (6) for incompressible materials ($J_3 = \lambda_1 \lambda_2 \lambda_3 = \lambda^2 \lambda_{th} = 1$) takes on the form of equation (9) (refs. 6, 7):

$$\frac{\sigma_{e-bi} \lambda}{\lambda^2 - 1/\lambda^4} = 2W_1 + 2W_2 \lambda^2 \tag{9}$$

Equation (9) can be rewritten in a more convenient form as equation (10):

$$\frac{\sigma_{e-bi} \lambda}{\lambda^4 - 1/\lambda^2} = \frac{2W_1}{\lambda^2} + 2W_2 \tag{10}$$

By plotting $\dfrac{\sigma_{e-bi} \lambda}{\lambda^4 - 1/\lambda^2}$ against $1/\lambda^2$, one can curve-fit the data points with a linear trend line, and determine $2W_2$ from the vertical intercept at $1/\lambda^2 = 0$; obtain $(2W_1 + 2W_2) = \mu$ from the vertical

7

intercept at $1/\lambda^2 = 1$, and obtain $2W_1$ from the slope of the curve-fitting straight line, or calculate from $2W_1 = \underbrace{(2W_1 + 2W_2)}_{\text{Determined}} - \underbrace{2W_2}_{\text{Determined}}$.

For a circular continuous specimen under radial biaxial tension, the entire specimen will be under the equal-biaxial stress field, which can be described by equation (9) or (10). However, in the biaxial balloon test, the equal-biaxial stress field occurs only in the ballooned specimen center.

Stress Difference Equations for the Current Problem

For a radially stretched circular hyperelastic sheet with a central circular hole, the remote boundary will be under the equal-biaxial stress field, but the traction free hole boundary will be under the uniaxial stress field in a tangential direction (fig. 6). Therefore, the uniaxial stress-difference equation (7) and the equal-biaxial stress-diffence equation (9) can be written for the hole boundary and remote boundary for stress calculations.

At the Hole Boundary

At the hole-boundary, the uniaxial stress difference equation (7) can be written in the following form for the Mooney material ($W_1 = 18.35$, $W_2 = 1.835$) lb/in^2 (refs 2, 3) as shown in equation (11):

$$
\begin{aligned}
\underbrace{\sigma_{uni}\lambda}_{\substack{\text{True stress}\\(J_3=1)}} \equiv \sigma_\theta(a)\lambda_\theta(a) \equiv \sigma_{\max}\lambda_{\max} &= 2\left(W_1 + \frac{W_2}{\lambda_{\max}}\right)\left(\lambda_{\max}^2 - \frac{1}{\lambda_{\max}}\right) \\
&= 2\left(18.35 + \frac{1.835}{\lambda_{\max}}\right)\left(\lambda_{\max}^2 - \frac{1}{\lambda_{\max}}\right)
\end{aligned}
\tag{11}
$$

In equation (11), $\sigma_{\max}[\equiv \sigma_\theta(a)]$ and $\lambda_{\max}[\equiv \lambda_\theta(a)]$ are respectively the tangential engineering stress and the tangential extension ratio at the hole boundary. To calculate the true stress ($\sigma_{\max}\lambda_{\max}$) from equation (11), the unknown $\lambda_{\max}$ can be determined from the equal-biaxial tensile tests by taking the ratio of the deformed hole-radius to the undeformed hole-radius according to equation (3). However, for the current analysis, values of $\lambda_{\max}$ were estimated from the Nastran large-strain large-deformation analysis.

At the Remote Boundary

At the remote boundary, the equal-biaxial stress difference equation (9) can be written for the Mooney material ($W_1 = 18.35$, $W_2 = 1.835$) lb/in^2 (refs 2, 3) in the following form as shown in equation (12):

$$
\begin{aligned}
\underbrace{\sigma_{e-bi}\lambda}_{\substack{\text{True stress}\\(J_3=1)}} \equiv \sigma_r(b)\lambda_r(b) \equiv \sigma_\infty\lambda_\infty &= 2\left(W_1 + W_2\lambda_\infty^2\right)\left(\lambda_\infty^2 - \frac{1}{\lambda_\infty^4}\right) \\
&= 2\left(18.35 + 1.835\lambda_\infty^2\right)\left(\lambda_\infty^2 - \frac{1}{\lambda_\infty^4}\right)
\end{aligned}
\tag{12}
$$

8

In equation (12), $\sigma_\infty[\equiv \sigma_r(b)]$ and $\lambda_\infty[\equiv \lambda_r(b)]$ are respectively the radial engineering stress and the radial extension ratio at the remote boundary. Because λ_∞ is specified, the true stress $\sigma_\infty \lambda_\infty$ at the remote boundary can be calculated from equation (12).

Stress Concentration Factor

The equal-biaxial stress concentration factor K is defined in equation (13):

$$K \equiv \frac{\text{Hole boundary true tangential stress}}{\text{Remote boundary true radial stress}} = \frac{\bar{\sigma}_\theta(a)}{\bar{\sigma}_r(b)} = \frac{\sigma_\theta(a)\lambda_\theta(a)}{\sigma_r(b)\lambda_r(b)} = \frac{\sigma_{max}\lambda_{max}}{\sigma_\infty \lambda_\infty} \qquad (13)$$

For classical linear elasticity, equation (13) will give a deformation-independent value of $K = 2$. Note that for the current radial loading, if $b \geq 10$ in., the remote boundary will be under the equal-biaxial stress field, and therefore, the radial and tangential stresses and extension ratios become identical; namely, $\sigma_r(b) = \sigma_\theta(b) \equiv \sigma_\infty$ and $\lambda_r(b) = \lambda_\theta(b) \equiv \lambda_\infty$. In the current analysis, the outer radius $b = 10$ in. was used for the circular finite-element model (fig. 3) for achieving the equal-biaxial stress field. By plotting K as a function of λ_∞, one can geometrically observe how the theoretically calculated and the Nastran calculated values of K increase with increasing λ_∞. Note that, to obtain the theoretical values of K, one has to calculate the true stresses $\{(\sigma_{max}\lambda_{max}),(\sigma_\infty\lambda_\infty)\}$ respectively from the large deformation constitutive equations $\{(11), (12)\}$.

Stretch Magnification Factor

For large deformations, measuring the extension ratio is much easier than measuring stresses because, no accurate large-deformation stress gages exist. Therefore, the stretch magnification factor K_λ can be introduced to study how the stretch magnification factor K_λ changes with stretching. Thus, one can avoid using large deformation constitutive equations. In the experiments or finite-element analysis, the remote extension ratio λ_∞ is specified. However, λ_{max} must be measured or calculated using finite-element analysis. Once λ_{max} is determined, then one can calculate the stretch magnification factor K_λ from equation (14):

$$K_\lambda = \frac{\text{Hole-boundary tangential extension ratio}}{\text{Remote radial extension ratio}} = \frac{\lambda_\theta(a)}{\lambda_r(b)} \equiv \frac{\lambda_{max}}{\lambda_\infty} \qquad (14)$$

Then one can plot the curves $\{K_\lambda \text{ against } \lambda_\infty\}$ and study how the value of K_λ changes with increasing λ_∞. When the strains approach zero, K_λ will approach the limit case of $K_\lambda = 1$.

Strain Magnification Factor

It is also a good idea to use the strain magnification factor K_ε and explore how the strain magnification factor K_ε changes with stretching. When λ_{max} is obtained from measurements (or finite-element analysis), then one can calculate the strain magnification factor K_ε from equation (15):

$$K_\varepsilon = \frac{\text{Hole boundary tangential strain}}{\text{Remote radial strain}} = \frac{\lambda_\theta(a)-1}{\lambda_r(b)-1} = \frac{\varepsilon_\theta(a)}{\varepsilon_r(b)} = \frac{\lambda_{max}-1}{\lambda_\infty-1} \equiv \frac{\varepsilon_{max}}{\varepsilon_\infty} \tag{15}$$

Then, one can plot the curve of K_ε as a function of λ_∞ for comparisons with the limit case of linear theory.

Limit Cases of the Strain Magnification Factor Based on the Large Deformation Theory

For small deformations, the uniaxial strain $\varepsilon_{max}(\equiv \varepsilon_{uni})$ and the equal-biaxial strain $\varepsilon_\infty(\equiv \varepsilon_{e-bi})$ can be calculated respectively from the large deformation stress equations (7) and (9) by expanding in the neighborhood of $\lambda \to 1$. Keep in mind that equations (7) and (9) are written for incompressible materials.

1. Limit Uniaxial Stress at the Hole Boundary

The large-deformation uniaxial stress equation (7) can be rearranged and expanded in terms of small uniaxial strain $\varepsilon_{uni}(\ll 1)$ as equation (16):

$$\begin{aligned}
\sigma_{max} \equiv \sigma_{uni} &= \left(2W_1 + \frac{2W_2}{\lambda}\right)\left(\lambda - \frac{1}{\lambda^2}\right) \xrightarrow{\lambda \to 1} \left(2W_1 + \frac{2W_2}{1+\varepsilon_{uni}}\right)\left[(1+\varepsilon_{uni}) - \frac{1}{(1+\varepsilon_{uni})^2}\right] \\
&= \left(2W_1 + 2W_2(1-\varepsilon_{uni}+...)\right)\left[(1+\varepsilon_{uni})-(1-2\varepsilon_{uni}+...)\right] \\
&\approx \underbrace{\left(2W_1 + 2W_2\right)}_{=\mu}3\varepsilon_{uni} = 3\mu\varepsilon_{uni}
\end{aligned} \tag{16}$$

From equation (16), uniaxial strain can be expressed in terms of uniaxial stress as equation (17):

$$\varepsilon_{uni} = \frac{\sigma_{uni}}{3\mu} \tag{17}$$

2. Limit Equal-Biaxial Stress at the Remote Boundary

The equal biaxial stress equation (9) can be rewritten and expanded in terms of small strain $\varepsilon_{e-bi}(\ll 1)$ as equation (18):

10

$$
\begin{aligned}
\sigma_{e-bi} &= \left(2W_1 + 2W_2\lambda^2\right)\left(\lambda - \frac{1}{\lambda^5}\right) \\
&= [2W_1 + 2W_2(1+\varepsilon_{e-bi})^2][(1+\varepsilon_{e-bi}) - (1+\varepsilon_{e-bi})^{-5}] \\
&= [(2W_1 + 2W_2) + 2W_2(2\varepsilon_{e-bi} + ...)](1 + \varepsilon_{e-bi} - 1 + 5\varepsilon_{e-bi} + ...) \\
&\approx \underbrace{(2W_1 + 2W_2)}_{=\mu}6\varepsilon_{e-bi} = 6\mu\varepsilon_{e-bi}
\end{aligned}
\tag{18}
$$

Equation (18) can be rewritten in a final form as equation (19):

$$
\varepsilon_{e-bi} = \frac{\sigma_{e-bi}}{6\mu}
\tag{19}
$$

3. The Resulting Limit Case of the Strain Magnification Factor

By substituting equations (17) and (19) into equation (15), the value of K_ε for the linear case can be calculated as equation (20):

$$
K_\varepsilon = \frac{\varepsilon_{max}}{\varepsilon_\infty} = \frac{\varepsilon_{uni}}{\varepsilon_{e-bi}} = \underbrace{\left(\frac{\sigma_{uni}}{3\mu}\right)}_{\varepsilon_{uni}}\underbrace{\left(\frac{6\mu}{\sigma_{e-bi}}\right)}_{1/\varepsilon_{e-bi}} = 2\frac{\sigma_{uni}}{\sigma_{e-bi}} = 2\underbrace{\left(\frac{\sigma_{max}}{\sigma_\infty}\right)}_{=K=2} = 4
\tag{20}
$$

Equation (20) shows that under the equal-biaxial stress field, for the linear-case of incompressible materials, the strain magnification factor $K_\varepsilon = 4$ is twice the linear-case of the stress concentration factor $K = 2$.

Limit Case of the Strain Magnification Factor Based on the Linear Theory

For small strain, the limit case of strain magnification factor K_ε given by equation (15) can also be calculated using the linear theory as shown in equation (21):

$$
K_\varepsilon = \frac{\varepsilon_{max}}{\varepsilon_\infty} \equiv \frac{\varepsilon_\theta(a)}{\varepsilon_r(b)} \xrightarrow[\text{case}]{\text{Linear}} \frac{\dfrac{1}{E}\overbrace{[\sigma_\theta(a) - v(0+0)]}^{\text{Uniaxial strain at hole boundary}}}{\underbrace{\dfrac{1}{E}\{\sigma_r(b) - v[\sigma_\theta(b) + 0]\}}_{\text{Equal-biaxial strain at remote boundary}}} = \frac{\sigma_\theta(a)}{\underbrace{\sigma_r(b) - v\sigma_\theta(b)}_{\sigma_r(b) = \sigma_\theta(b)}} = \frac{\sigma_\theta(a)}{(1-v)\sigma_r(b)}
\tag{21}
$$

Equation (21) shows that the value of K_ε is a function of Poisson's ratio v. For incompressible materials (for example, hyperelastic materials), the Poisson's ratio is practically $v = 0.5$, then equation (21) takes on the form of equation (22):

11

$$K_\varepsilon = \frac{\sigma_\theta(a)}{\underbrace{(1-\nu)\sigma_r(b)}_{\nu-\text{dependent}}} \xrightarrow[\substack{\text{Incompressible} \\ \nu=0.5}]{} \frac{1}{0.5}\frac{\sigma_\theta(a)}{\sigma_r(b)} = \frac{1}{0.5}\underbrace{\left(\frac{\sigma_{max}}{\sigma_\infty}\right)}_{=K=2} = 4 \tag{22}$$

Thus, for incompressible materials ($\nu = 0.5$), both the linear theory and the limit case of the large deformation theory give the identical equal-biaxial strain magnification factor of $K_\varepsilon = 4$ [eqs. (20), (22)].

Numerical Results

For the calculations of $\{K, K_\lambda, K_\varepsilon\}$ [eqs. (13), (14), (15)], values of $\{\lambda_\infty, \lambda_{max}\}$ are needed. The remote extension ratio λ_∞ is specified and is known. However, the unknown $\lambda_{max}[\equiv \rho(a)/a]$ must be determined from experiment. Namely, by simply measuring the deformed hole radius $\rho(a)$ and taking the ratio $\rho(a)/a$ to obtain λ_{max} according to equation (3). The geometrical measurement of λ_{max} is much simpler than measuring the large deformation stress σ_{max} at the small hole boundary because no miniature strain gages can operate under very large deformations. In the present report, values of λ_{max} were estimated by using Nastran large-strain large-deformation analysis.

Nastran Data

The major data generated from Nastran large-strain large-deformation analysis are listed in table 1. The Nastran-generated K listed in table 1 will be plotted in the subsequent section (Plots of K Curves), after the corresponding theoretical values of K are calculated for comparisons.

Table 1. Nastran generated data for calculating the equal-biaxial stress concentration factor K, and the stretch and strain magnification factors $\{K_\lambda, K_\varepsilon\}$; Mooney material ($W_1 = 18.35$, $W_2 = 1.835$) lb/in^2; ($a = 0.5$, $b = 10$, $t = 0.0625$) in.

λ_∞	σ_∞, lb/in^2	λ_{max}	σ_{max}, lb/in^2	K	K_λ	K_ε
1.25	48.26	2.06	141.71	2.94	1.65	4.24
1.50	90.78	3.09	338.69	3.73	2.06	4.18
1.70	128.61	3.92	547.36	4.26	2.31	4.17
1.98	192.41	5.18	956.96	4.97	2.62	4.28
2.10	224.62	5.79	1192.26	5.31	2.76	4.35
2.35	302.75	7.22	1850.38	6.11	3.07	4.61

Average = 4.3048

Figure 7 shows plots of the Nastran-generated tangential extension ratios $\lambda_\theta(r)$ as functions of radial distance r under different levels of the remote radial extension ratios λ_∞. Note that for each level of λ_∞, the corresponding $\lambda_\theta(r)$ increases toward the hole and reached the maximum value $\lambda_\theta(a) \equiv \lambda_{max}$ at the hole-boundary.

Figure 8 shows the Nastran-generated hole-boundary tangential extension ratio $\lambda_{max}[\equiv \lambda_\theta(a)]$ plotted as a function of the remote radial extension ratio $\lambda_\infty[\equiv \lambda_r(b)]$. Note that the λ_{max} curve is practically a straight line up to $\lambda_\infty = 1.75$, and then slightly bend upward as λ_∞ further increases. At the remote

stretching of $\lambda_\infty = 2.35$, the hole-boundary extension ratio λ_{max} can reach as large as $\lambda_{max} = 7.22$ (fig. 7).

Theoretical Predictions of the Stress Concentration Factor

In the calculations of theoretical stress concentration factors K, the known remote extension ratios λ_∞ and the Nastran-estimated hole boundary extension ratio λ_{max} were used to calculate remote true (Cauchy) radial stresses $\sigma_\infty \lambda_\infty$ and hole-boundary true (Cauchy) tangential stresses $\sigma_{max} \lambda_{max}$. The results of calculations are listed in table 2 with Nastran data (table 1) included for comparison.

Table 2. Calculations of stress concentration factors K using equations {(11), (12)} compared with Nastran K; Mooney material ($W_1 = 18.35$, $W_2 = 1.835$) lb/in^2; ($a = 0.5$, $b = 10$, $t = 0.0625$) in.

Equal-biaxial for remote boundary

$$\underbrace{\sigma_{e-bi}\lambda_\infty}_{\text{True stress}} = \underbrace{2\left(18.35 + 1.835 \times \lambda_\infty^2\right)}_{A_\infty} \underbrace{\left(\lambda_\infty^2 - \frac{1}{\lambda_\infty^4}\right)}_{B_\infty}$$

Uniaxial for hole boundary

$$\underbrace{\sigma_{uni}\lambda_{max}}_{\text{True stress}} = \underbrace{2\left(18.35 + \frac{1.835}{\lambda_{max}}\right)}_{A_{max}} \underbrace{\left(\lambda_{max}^2 - \frac{1}{\lambda_{max}}\right)}_{B_{max}}$$

|<-----------------Equal-biaxial at remote boundary--------------->|<---------------------Uniaxial at hole boundary--------------------->|

λ_∞	λ_∞^2	A_∞	B_∞	$\sigma_\infty \lambda_\infty$	λ_{max}	λ_{max}^2	A_{max}	B_{max}	$\sigma_{max} \lambda_{max}$	K
$[\equiv \lambda_r(b)]$				(Equal-biaxial)		$[\equiv \lambda_\theta(a)]$			(Uniaxial) $\left(= \dfrac{\sigma_{max}\lambda_{max}}{\sigma_\infty\lambda_\infty}\right)$	
1.01	1.0201	40.7438	0.0591	2.4088	1.04	1.0816	40.2288	0.1201	4.8315	2.0058
									Nastran =	2.0000
1.25	1.5625	42.4344	1.1529	48.9226	2.06	4.2436	38.4816	3.7582	144.5088	2.9538
									Nastran =	2.9364
1.50	2.2500	44.9575	2.0525	92.2753	3.09	9.5481	37.8877	9.2245	349.4951	3.7875
									Nastran =	3.7309
1.70	2.8900	47.3063	2.7703	131.0526	3.92	15.3664	37.6362	15.1113	568.7319	4.3397
									Nastran =	4.2560
1.98	3.9204	51.0879	3.8553	196.9591	5.18	26.7289	37.4099	26.5355	992.6904	5.0401
									Nastran =	4.9735
2.10	4.4100	52.8847	4.3586	230.5033	5.78	33.4084	37.3349	33.2354	1,240.8403	5.3832
									Nastran =	5.3079
2.35	5.5225	56.9676	5.4897	312.7350	7.22	52.1284	37.2083	51.9899	1,934.4558	6.1856
									Nastran =	6.1119

Plots of the Stress Concentration Factor

Figure 9 shows the plots of theoretical K listed in table 2 and Nastran-generated K of table 1. Note that, the two K-curves calculated from both the Blatz-Ko large deformation theory and from the Nastran large-strain large-deformation analysis are extremely close. Note also that, unlike the classical linear theory which gives material and deformation independent $K = 2$, the value of K for hyperelastic material increases almost linearly (with slight waving) with increased stretching, and can exceed $K = 6$ at the remote extension ratio of $\lambda_\infty = 2.35$.

Figure 10 compares the K-curves based on current analysis and K-curves obtained by earlier researchers. Note that Yang's K-curve [theoretically calculated using $(W_2/W_1) = 0.1$ (ref. 8)], which only ends at $(K = 5.4, \lambda_\infty = 2.1)$, is very close to the K curves calculated from the Blatz-Ko theory and the Nastran large-strain and large-deformation analysis. The Segal-Klosner's K-curve [experimentally obtained using square sheet (6.5 in.$\times$ 6.5 in.) of natural rubber (ref. 9)] is a straight line only up to $K \approx 4$ at the remote extension ratio $\lambda_\infty = 1.62$. The last data point falls on the vicinity of the K-curves calculated from Nastran and the Blatz-Ko theory (fig. 10). However, Oden's K-curve (refs. 10, 11) is somewhat off and gives higher K values. Keep in mind that Oden's K-curve was finite-element-generated, and the discrepancy could be attributed to the use of a much coarser finite-element model with a smaller remote radius of $b = 5$ in. (ref. 11), and the use of a slightly lower value of $(W_2/W_1) = 0.08$. In the current analysis, it was found that the value of K was extremely sensitive to the finite-element mesh sizes and the dimension of remote radius b.

Plots of the Stretch and Strain Magnification Factors

Figure 11 shows the stretch magnification factor K_λ (data from table 1) plotted as a function of the remote extension ratio λ_∞. Note that, the value of K_λ starts from $K_\lambda = 1$ and increases convex-upwardly with increasing λ_∞, and then reached the value of $K_\lambda = 3.07$ at $\lambda_\infty = 2.35$.

Figure 12 shows the strain magnification factor K_ε (data from table 1) plotted as a function of the remote extension ratio λ_∞. Note that, the value of K_ε starts from the linear value of $K_\varepsilon = 4$, and increases nonlinearly with increasing λ_∞, and reached the value of $K_\varepsilon = 4.61$ at $\lambda_\infty = 2.35$.

Numerical Results of Hole-Size Effect on the Stress Concentration Factor

After the above stress concentration studies, additional studies were conducted to investigate the hole-size effect on the stress concentration factor K in the equal-biaxial strain field. The hole-sizes considered are $a = (0.5, 0.25, 0.125, 0.05)$ in.

Equal-Biaxial Stress Concentration Factor

The theoretically-calculated K-values and corresponding Nastran generated K-values are listed in table 3.

Table 3. Theoretical equal-biaxial stress concentration factors K [eqs. (11), (12)] compared with Nastran-generated K ; Mooney material (W_1 = 18.35, W_2 = 1.835) lb/in^2; [a = (0.5, 0.25, 0.125, 0.05), b = 10, t = 0.0625] in.

$$\underbrace{\sigma_{e-bi}\lambda_\infty}_{\text{True stress}} = 2\left(18.35 + 1.835 \times \lambda_\infty^2\right)\left(\lambda_\infty^2 - \frac{1}{\lambda_\infty^4}\right) \qquad \underbrace{\sigma_{uni}\lambda_{max}}_{\text{True stress}} = 2\left(18.35 + \frac{1.835}{\lambda_{max}}\right)\left(\lambda_{max}^2 - \frac{1}{\lambda_{max}}\right)$$

|<-----Equal-biaxial at remote boundary----->|<-----Uniaxial at hole boundary------>| | | |
λ_∞	$\sigma_\infty\lambda_\infty$ (Equal biaxial)	λ_{max}	$\sigma_{max}\lambda_{max}$ (Uniaxial)	K $(\sigma_{max}\lambda_{max})/(\sigma_\infty\lambda_\infty)$	K (Nastran)	ΔK (% difference)
			a = 0.5 in.			
1.01	2.3910	1.04	4.8299	2.0200	2.0000	1.00
1.25	48.9226	2.06	144.5088	2.9538	2.9364	0.59
1.50	92.2753	3.09	349.4951	3.7875	3.7309	1.52
1.70	131.0526	3.91	568.7319	4.3397	4.2560	1.97
1.98	196.9591	5.17	992.6904	5.0401	4.9735	1.34
2.10	230.5033	5.78	1240.8403	5.3832	5.3079	1.42
2.35	312.7350	7.22	1934.4558	6.1856	6.1119	1.21
			a = 0.25 in.			
1.01	2.3910	1.04	4.8299	2.0200	2.0000	1.00
1.25	48.9226	2.04	141.3455	2.8892	2.9600	2.39
1.50	92.2753	3.11	354.1997	3.8386	3.7800	1.55
1.70	131.0526	3.90	562.8685	4.2950	4.3100	0.35
1.98	196.9591	5.18	996.5380	5.0596	5.0600	0.01
2.10	230.5033	5.81	1253.7462	5.4392	5.4200	0.35
2.35	312.7350	7.28	1966.6484	6.2885	6.2500	0.62
			a = 0.125 in.			
1.01	2.3910	1.04	4.8299	2.0200	1.9900	1.51
1.25	48.9226	2.01	136.4813	2.7897	2.8700	2.80
1.50	92.2753	3.03	335.5472	3.6364	3.6500	0.37
1.70	131.0526	3.86	549.7804	4.1952	4.1500	1.09
1.98	196.9591	5.13	977.3639	4.9622	4.8800	1.68
2.10	230.5033	5.66	1189.8801	5.1621	5.2200	1.11
2.35	312.7350	7.17	1907.8306	6.1005	6.0100	1.51
			a = 0.05 in.			
1.01	2.3910	1.03	3.6247	1.5160	1.6000	5.25
1.25	48.9226	1.83	108.4702	2.2172	2.1500	3.13
1.50	92.2753	2.65	253.0796	2.7427	2.6700	2.72
1.70	131.0526	3.33	407.8317	3.1120	3.0200	3.05
1.98	196.9591	4.35	701.7895	3.5631	3.5000	1.80
2.10	230.5033	4.84	869.7430	3.7733	3.7300	1.16
2.35	312.7350	6.06	1363.8403	4.3610	4.2600	2.37

Plots of Hole-Size Effect Data

Figure 13 shows the plots of λ_{max} as functions of λ_{∞} for different hole sizes. The λ_{max}-curves for the hole-sizes $a = (0.5, 0.25, 0.125)$ in. almost form a single curve, indicating that under those hole-sizes, there is practically no hole-size effect on the stress concentration factor K. The λ_{max}-curve for the hole-size $a = 0.05$ in. is somewhat off from the group of λ_{max}-curves, and has a lower slope, showing the effect of the hole-size on K.

Figure 14 shows the stress concentration factors K plotted as functions of λ_{∞} for different hole sizes. The K curves for hole-sizes $a = (0.5, 0.25, 0.125)$ in. are very close, indicating that under those hole-sizes, there is practically no hole-size effect on K. The K-curve for the hole-size $a = 0.05$ in. is considerably off from the group K-curves, and has lower slope, indicating the existence of hole-size effect on K.

Figure 15 shows the hole-boundary tangential extension ratio λ_{max} plotted as functions of hole-radius a for different levels of remote extension ratios λ_{∞}. As shown in table 2, λ_{max} is the key control factor affecting the stress concentration factor K, and therefore, it is important to first examine the behavior of the λ_{max}-curves (fig. 15) before the K-curves are presented. As shown in figure 15, the λ_{max}-curves for different levels of λ_{∞} are practically horizontal in the hole-size range of $(0.125 \leq a \leq 0.5)$ in., indicating that there is no hole-size effect. When the hole-size is decreased from $a = 0.125$ in., the value of λ_{max} for each case of λ_{∞} starts to decrease with a decreasing-hole radius a, and finally down to $\lambda_{max} = 1$ at $a = 0$ in. (no hole). The pictorial shapes of λ_{max} suggest that the corresponding K-curves will have very similar geometrical shapes.

Figure 16 shows the equal-biaxial stress concentration factors K plotted as functions of hole-radius a for different levels of remote extension ratios λ_{∞}. Note that, the geometrical shapes of the K-curves are very similar to those of the corresponding λ_{max}-curves shown in figure 12. The K-curves in the range of $(0.125 \leq a \leq 0.5)$ in. for all levels of λ_{∞} are practically horizontal, indicating that there is no hole-size effect on K. When the hole-size is decreased from $a = 0.125$ in., the value of K for each case of λ_{∞} starts to decrease with decreasing hole radius a and finally down to $K = 1$ (no stress concentration) at $a = 0$ in. (no hole). Thus, for the current special case of Mooney material ($W_1 = 18.35$, $W_2 = 1.835$) lb/in^2, the hole-size effect on K will appear only in the small region $(0 \leq a \leq 0.125)$ in.

Concluding Remarks

1. For the linear elasticity theory, the equal-biaxial stress concentration factor K is $K = 2$, and is independent of strains and material properties.

2. The strain magnification factor K_{ε} for linear case is $K_{\varepsilon} = 4 \ (= 2K)$ for incompressible materials.

3. For large deformations, the equal-biaxial stress concentration factors K calculated from the Blatz-Ko large-deformation theory and from the Nastran large-strain large deformation analysis using Mooney material ($W_1 = 18.35, W_2 = 1.835$) lb/in^2 are extremely close, both of which compare fairly well with the K-values obtained by earlier authors.

4. For the hyperelastic Mooney material considered, the equal-biaxial stress concentration factor K is a strong function of stretching and material property. At the remote extension ratio of $\lambda_\infty = 2.35$, the value of K can exceed $K = 6$.

5. For the hyperelastic Mooney material considered, the equal-biaxial stretch magnification factor K_λ is a function of stretching, and can increases from $K_\lambda = 1$ (limit case) up to $K_\lambda = 3.07$ at the remote extension ratio of $\lambda_\infty = 2.35$.

6. For the hyperelastic Mooney material considered, the equal-biaxial strain magnification factor K_ε is a weak function of stretching, and can increase from $K_\varepsilon = 4$ (linear case) up to $K_\varepsilon = 4.61$ at the remote extension ratio of $\lambda_\infty = 2.35$.

7. For the hyperelastic Mooney material considered, the hole-size effect on the equal-biaxial stress concentration factor K starts to appear when the hole radius a is less than $a = 0.125$ in. Namely, at the hole radius $a = 0.125$ in. the value of K (associated with any remote extension ratio λ_∞) starts to decrease gradually and finally down to the lowest limit value of $K = 1$ (no stress concentration) as the hole-radius a shrinks to zero ($a = 0$ in.).

Figures
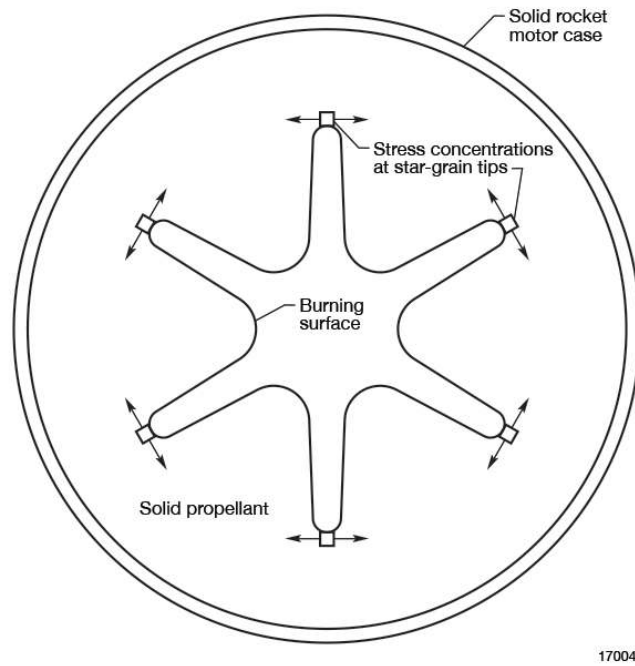
Figure 1. Tensile stress critical regions in a solid rocket star grain due to internal pressure and inclusion effect.
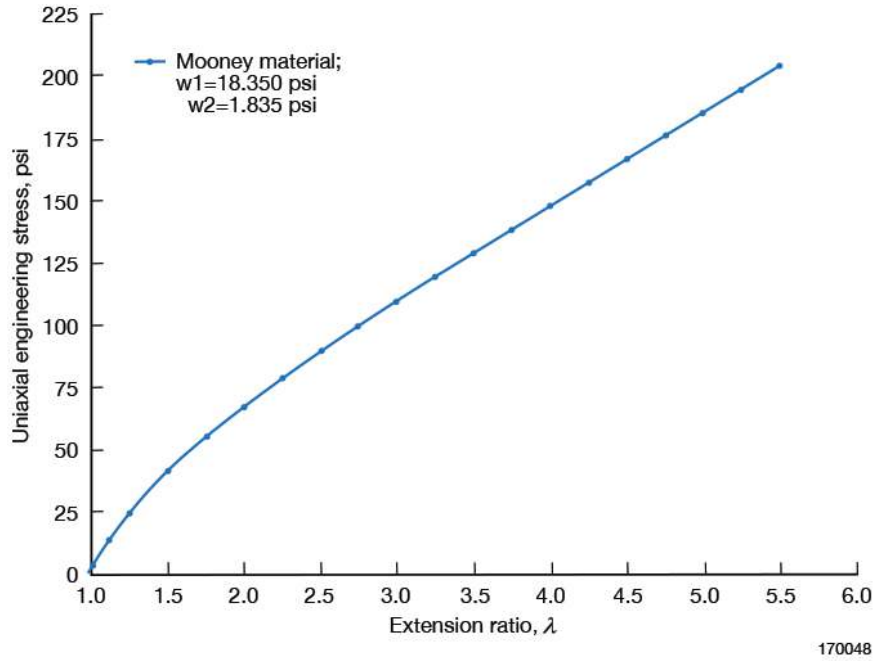
Figure 2. Uniaxial stress-strain curve of the Mooney material (W_1 = 18.35, W_2 = 1.835) lb/in² used in the analysis.
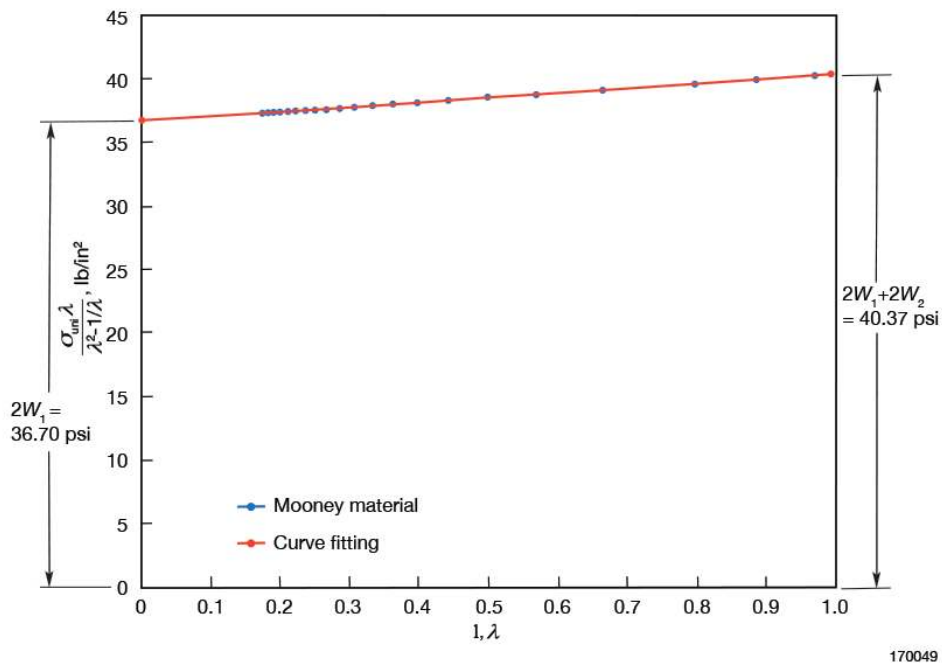
Figure 3. Reduced plot of the data of figure 1 for determining Mooney material constants (W_1 = 18.35, W_2 = 1.835) lb/in².
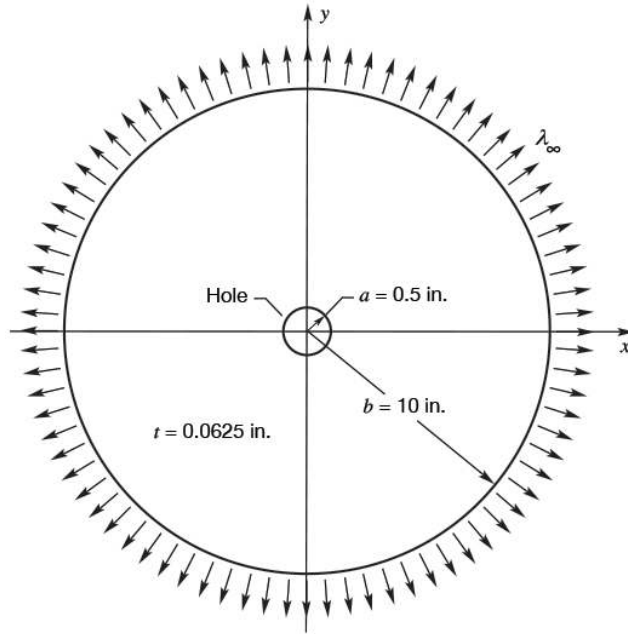
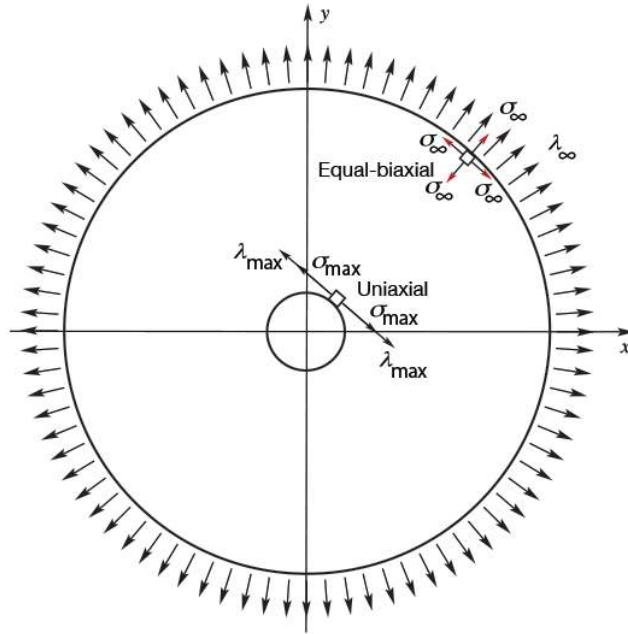Figure 4. Hyperelastic circular sheet containing a central circular hole subjected to remote radial stretching ($a = 0.5$, $b = 10$, $t = 0.0625$) in.; Mooney material ($W_1 = 18.35$, $W_2 = 1.835$) lb/in^2.
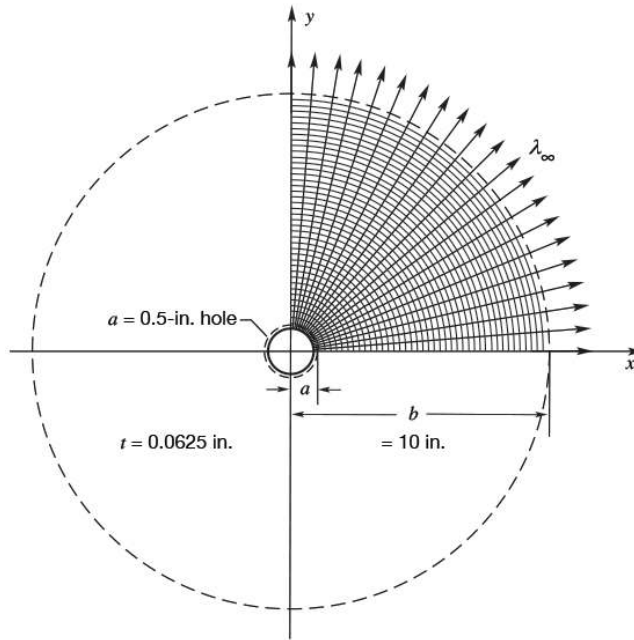
Figure 5. Finite-element quarter model for hyperelastic circular sheet containing a central circular hole ($a = 0.5$, $b = 10$, $t = 0.0625$) in.; Mooney material ($W_1 = 18.35$, $W_2 = 1.835$) lb/in^2.

Figure 6. In a radially stretched circular hyperelastic sheet with a central circular hole, the outer boundary will be under equal-biaxial tension, while the traction free hole boundary will be under uniaxial tension in a tangential direction.
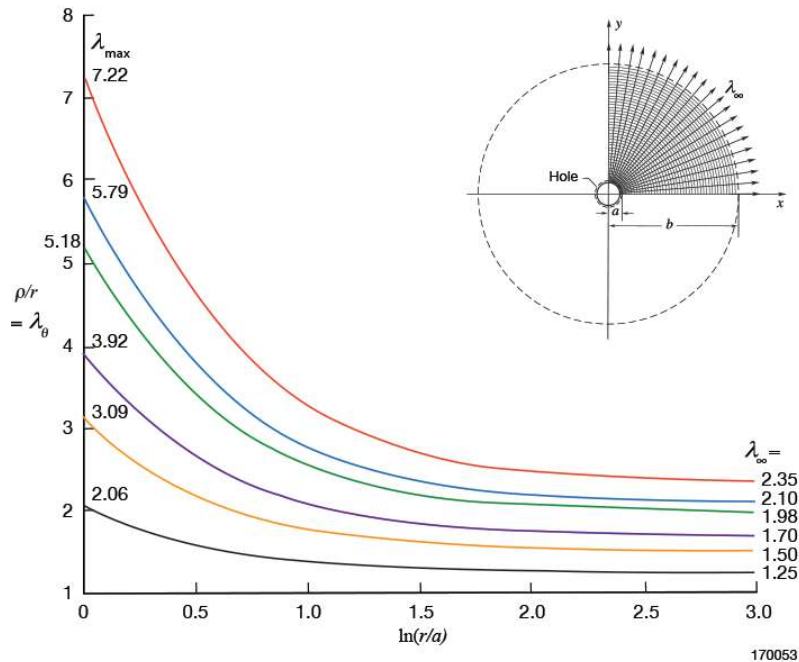
Figure 7. Radial variations of tangential extension ratios $\lambda_\theta (= \rho/r)$ for different remote radial extension ratios $\lambda_\infty [\equiv (d\rho/dr)_{r=b}]$; Mooney material ($W_1 = 18.35$, $W_2 = 1.835$) lb/in^2; ($a = 0.5$, $b = 10$, $t = 0.0625$) in.
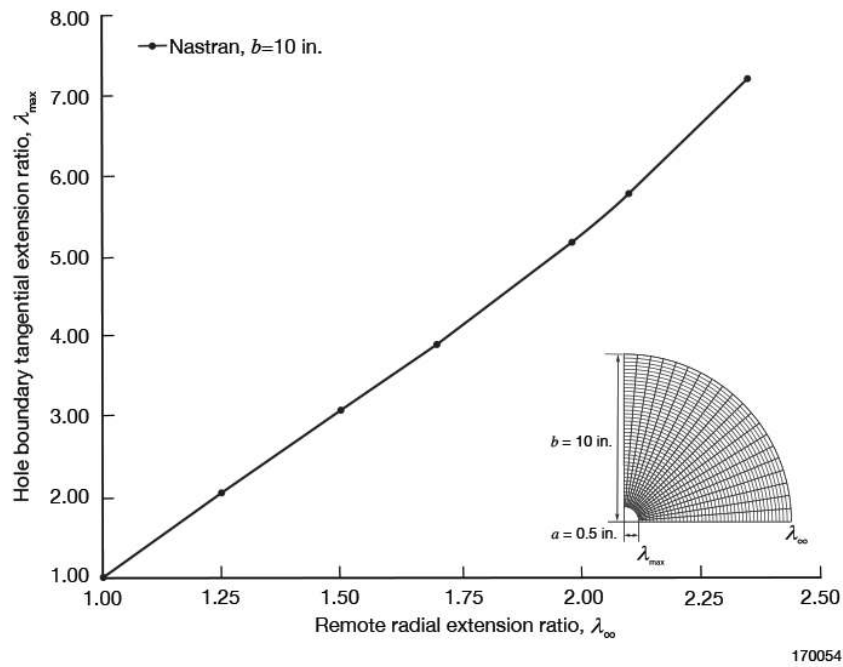
Figure 8. Plot of a Nastran-generated hole-boundary tangential extension ratio λ_{max} as a function of the remote radial extension ratio λ_∞; Mooney material (W_1 = 18.35, W_2 = 1.835) lb/in^2; (a = 0.5, b = 10, t = 0.0625) in.
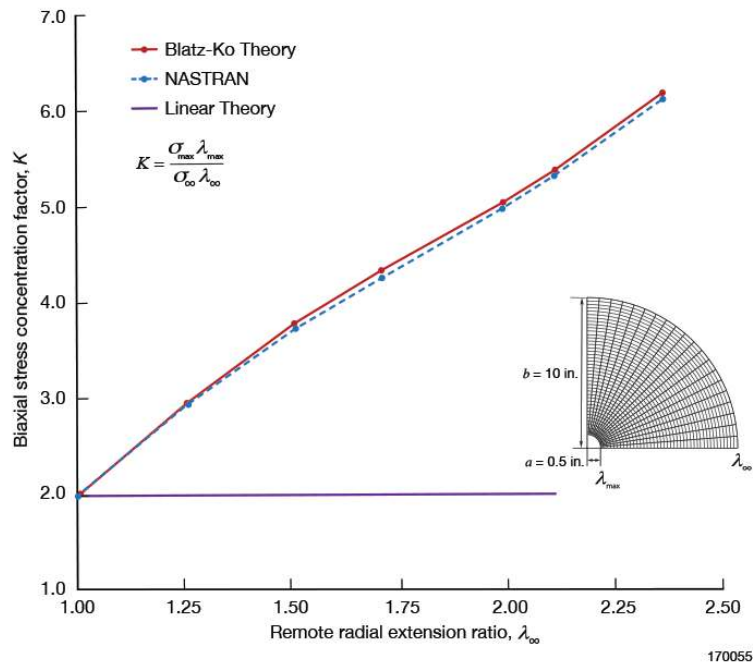
Figure 9. Comparison of theoretical and Nastran stress concentration curves for Mooney material (W_1 = 18.35, W_2 = 1.835) lb/in^2; (a = 0.5, b = 10, t = 0.0625) in.
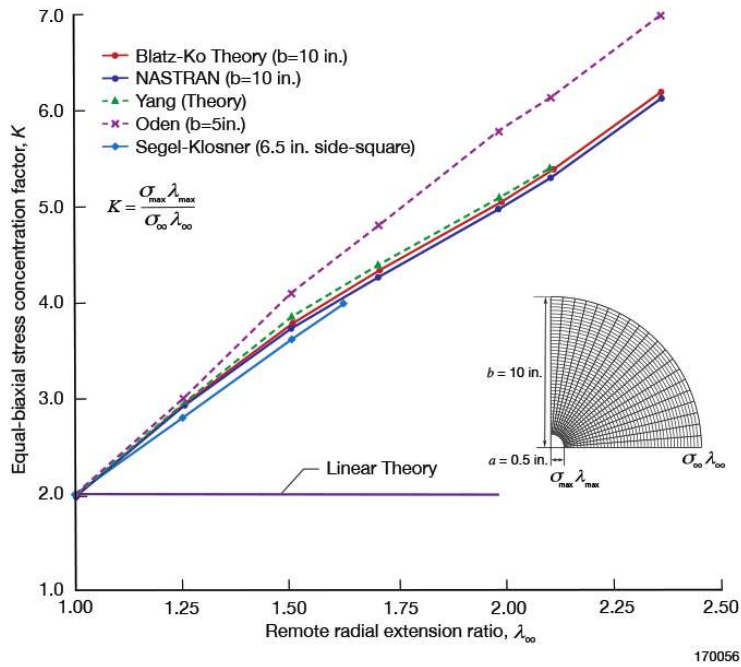
22

Figure 10. Comparison of stress concentration curves based on current analysis and earlier authors; Yang (ref. 8), Segal-Klosner (ref.9), and Oden (refs. 10, 11) for Mooney material (W_1 = 18.35, W_2 = 1.835) lb/in^2.
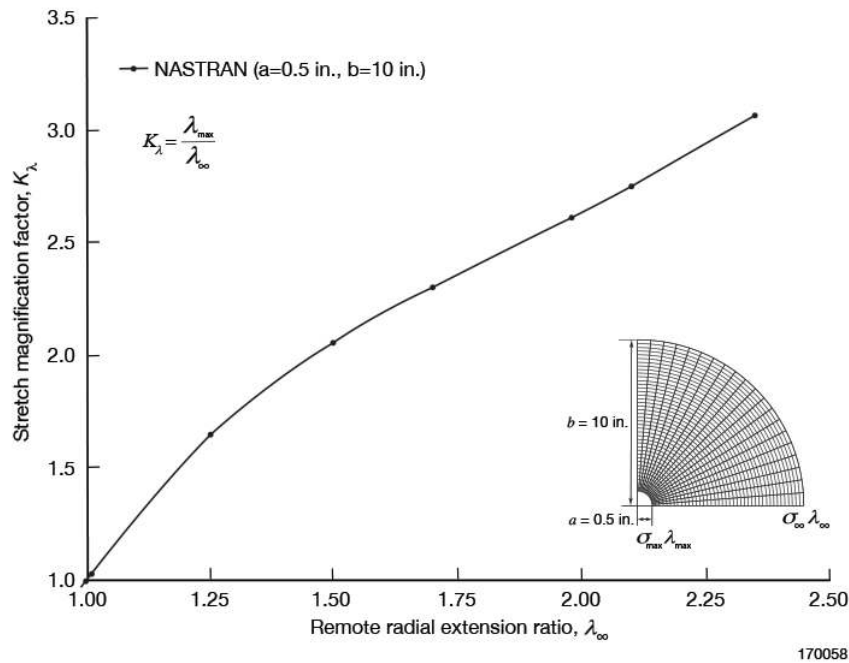
Figure 11. Nastran-generated stretch magnification curves; Mooney material (W_1 = 18.35, W_2 = 1.835) lb/in^2; (a = 0.5, b = 10, t = 0.0625) in.
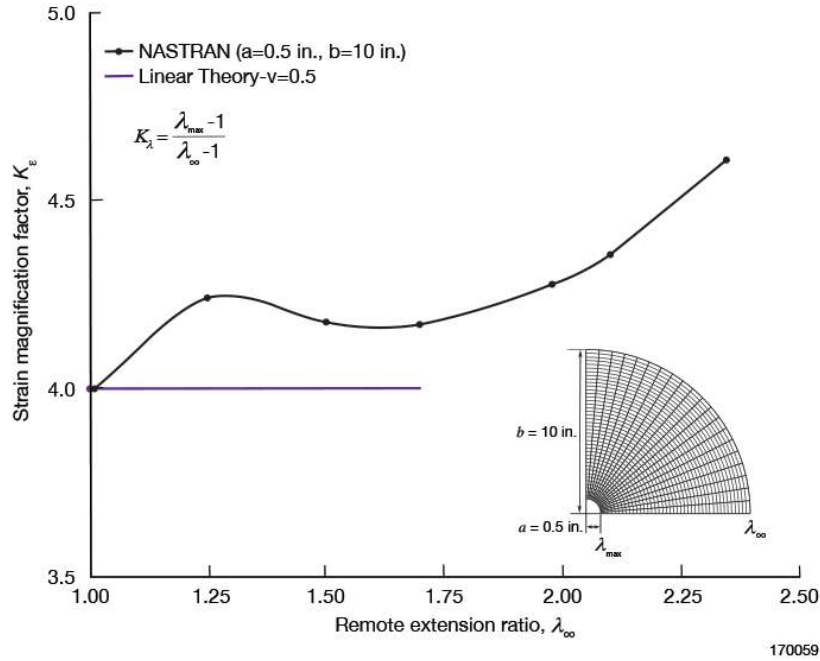
23

Figure 12. Nastran-generated strain magnification curves; Mooney material (W_1 = 18.35, W_2 = 1.835) lb/in^2; (a= 0.5, b = 10, t = 0.0625) in.
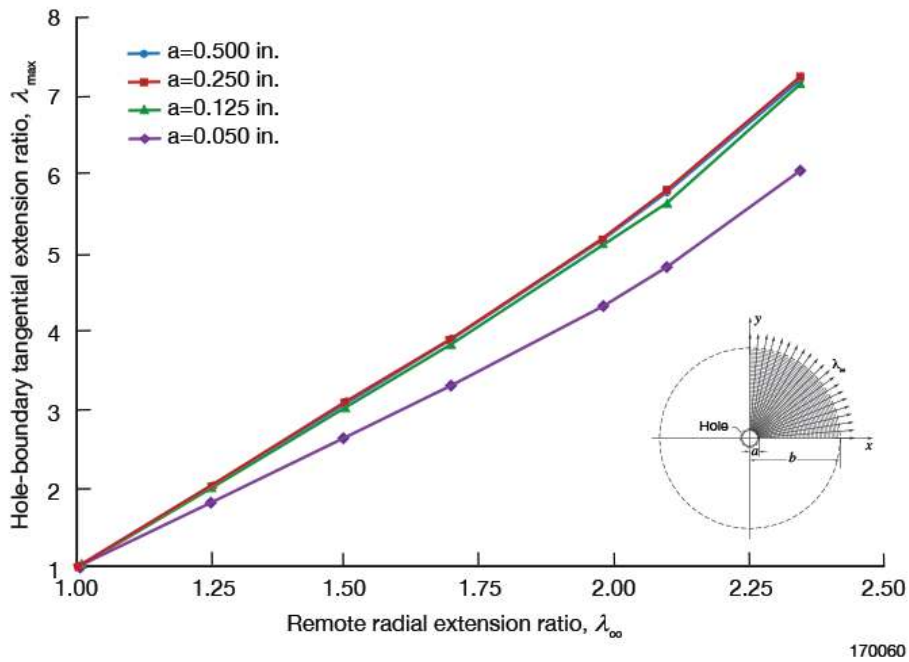

Figure 13. Plots of Nastran-generated hole-boundary tangential extension ratios λ_{max} as functions of the remote extension ratio λ_∞ for different hole sizes; Mooney material (W_1 = 18.35, W_2 = 1.835) lb/in^2; [a = (0.5, 0.25, 0.125, 0.05), b =10, t = 0.0625] in.
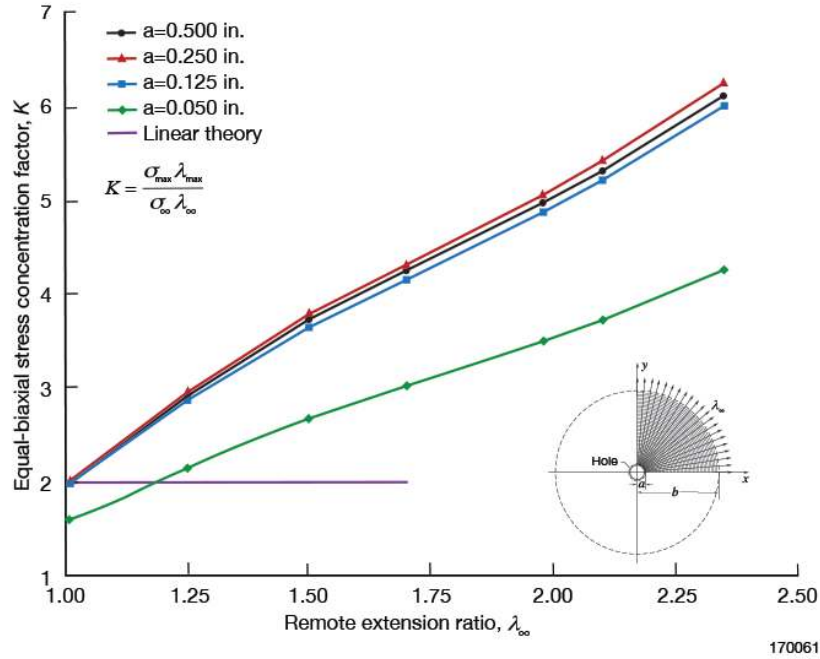
Figure 14. Plots of Nastran-generated equal-biaxial stress concentration factors K as functions of the remote extension ratio λ_∞ for different hole sizes; Mooney material ($W_1 = 18.35$, $W_2 = 1.835$) lb/in^2; [$a = (0.5, 0.25, 0.125, 0.05)$, $b = 10$, $t = 0.0625$] in.
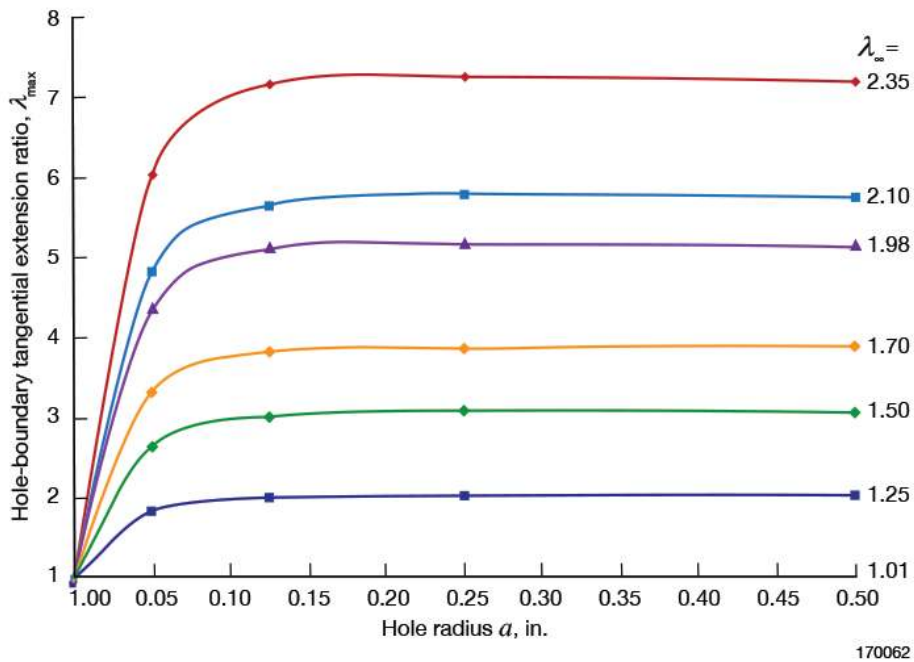

Figure 15. Variation of the hole-boundary extension ratio λ_{max} with hole-radius a under different remote extension ratios λ_∞; Mooney material ($W_1 = 18.35$, $W_2 = 1.835$) lb/in^2; [$a = (0.5, 0.25, 0.125, 0.05)$, $b = 10$, $t = 0.0625$] in.
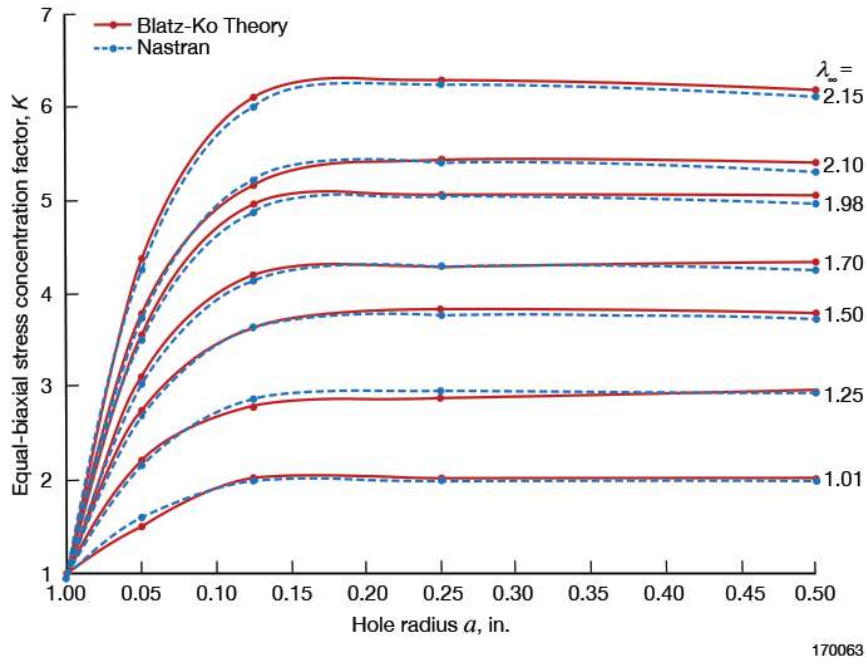
25

Figure 16. Variation of equal-biaxial stress concentration factors K with hole-radius a under different remote extension ratios λ_∞; comparisons of theoretically-generated K-curves and Nastran-generated K-curves; Mooney material (W_1 = 18.35, W_2 = 1.835) lb/in^2 ; [a = (0.5, 0.25, 0.125, 0.05), b = 10, t = 0.0625] in.

References

1. Sreekantamurthy, Thammaiah, Travis L. Turner, James B. Moore, and Ji Su, "Elastomeric Structural Attachment Concepts for Aircraft Flap Noise Reduction - Challenges and Approaches to Hyperelastic Structural Modeling and Analysis," AIAA-2014-0509, January 2014.

2. Peterson, Rudloph Earl, *Stress Concentration Factors: Charts and Relations Useful in Making Strength Calculations for Machine Parts and Structural Elements*, John Wiley & Sons, New York, 1974.

3. Rivlin, R. S., and A. G. Thomas, "Large Elastic Deformations of Isotropic Materials, VIII. Strain Distribution around a Hole in a Sheet," *Philosophical Transactions of the Royal Society of London. Series A, Mathematical and Physical Sciences*, Vol. 243, No. 865, pp. 289-298, April 24, 1951.

4. Rivlin, R. S., and D. W. Saunder, "Large Elastic Deformations of Isotropic Materials, VII. Experiments on the Deformation of Rubber," *Philosophical Transactions of the Royal Society of London. Series A, Mathematical and Physical Sciences*, Vol. 243. No. 865, pp. 251-288, April 24, 1951.

5. *MSC. NASTRAN 2005 Quick Reference Guide*, The MacNeal Schwendler Corporation, Newport Beach, California, 2005.

6. Blatz, Paul J., and William L. Ko, "Application of Finite Elastic Theory to the Deformation of Rubbery Materials," *Transactions of the Society of Rheology*, Vol. 6, pp. 223-251, 1962.

7. Ko, William L., "Application of Finite Elastic Theory to the Behavior of Rubber-Like Materials," Ph.D. Dissertation, California Institute of Technology, Pasadena, California, June 1963.

8. Yang, W. H., "Stress Concentration in a Rubber Sheet Under Axially Symmetric Stretching," Journal of Applied Mechanics, Vol. 34, pp. 942-946, December 1967.

9. Segal, Alexander, and Jerome M. Klosner, "Stress Concentration in Elastomeric Sheet Subject to Large Deformations," PIBAL Report No. 70-11, March 1970.

10. Oden, J. T., and J. E. Key, "Analysis of Finite Deformations of Elastic Solids by the Finite-Element Method," Proceedings of the Symposium on High Speed Computing of Elastic Structures, Liege, Belgium, August 23-28, 1970.

11. Oden, J. T., *Finite Elements of Nonlinear Continua*, McGraw-Hill Book Company, New York, 1972.